

Vortex detection and quantum transport in mesoscopic graphene Josephson junction arrays

C. L. Richardson¹, S. D. Edkins¹, G. R. Berdiyrov^{2,3}, C. J. Chua¹, J. P. Griffiths¹, G. A. C. Jones¹, M. R. Buitelaar^{1,4}, V. Narayan¹, F. Sfigakis¹, C. G. Smith¹, L. Covaci², M. R. Connolly^{1,5}

¹*Cavendish Laboratory, Department of Physics, University of Cambridge, Cambridge CB3 0HE, UK*

²*Departement Fysica, Universiteit Antwerpen, Groenenborgerlaan 171, 2020 Antwerpen, Belgium*

³*Department of Physics, King Fahd University of Petroleum and Minerals, Dhahran 31261, Kingdom of Saudi Arabia*

⁴*Department of Physics and Astronomy, University College London, Gower Street, London WC1E 6BT, UK and*

⁵*National Physical Laboratory, Hampton Road, Teddington TW11 0LW, UK*

(Dated: December 3, 2024)

We explore the interplay between normal-state and superconducting phase coherence in mesoscopic Josephson junction arrays created by patterning superconducting disks on monolayer graphene. We find that the mean conductance and universal conductance fluctuations are both enhanced below the critical temperature and field of the superconductor, with greater enhancement away from the graphene Dirac point. We also observe features in the magnetoconductance at rational fractions of flux quanta per array unit cell, which we attribute to the formation of vortices in the arrays. The applied fields at which the features occur are well described by Ginzburg-Landau simulations that take into account the number of unit cells in the array.

Superconducting vortices in a two-dimensional gas of chiral massless Dirac fermions are predicted to harbour excitations that resemble hypothetical elementary particles known as Majorana zero modes [1, 2]. Developing ways to create, control, and interfere vortices in candidate Dirac conductors—such as graphene and the surface states of three-dimensional topological insulators—is therefore important for detecting non-Abelian statistics and for implementing topologically protected quantum information processing [3].

In the absence of intrinsic pairing of electrons through the Cooper channel, attention has focused on using the proximity effect to induce a Dirac condensate in these materials [4]. In the proximity effect, a normal metal/superconductor interface generates phase-correlated quasiparticle pairs via Andreev reflection, which opens an effective gap in the normal metal. These pairs communicate phase information between superconductors in Josephson junctions, leading to supercurrent flow. Using graphene as the normal conductor also allows the normal-state resistance to be tuned via the carrier density [5, 6]. This leads to a superconducting-to-insulating transition in disordered arrays [7], and the addition of flux pinning in ordered arrays creates a superconducting glass state at low temperatures [8, 9]. The presence of flux vortices in such devices causes a phase frustration between array islands, which interacts with the normal-state quantum interference as well as Andreev corrections to the conductance in these mesoscopic, two-dimensional devices.

In this Letter we study how the mean value and fluctuations of the conductance of monolayer graphene are modified in the presence of ordered arrays of superconducting disks. We find that both are enhanced below the critical temperature and field of the superconductor due to the proximity effect, with greater enhancement

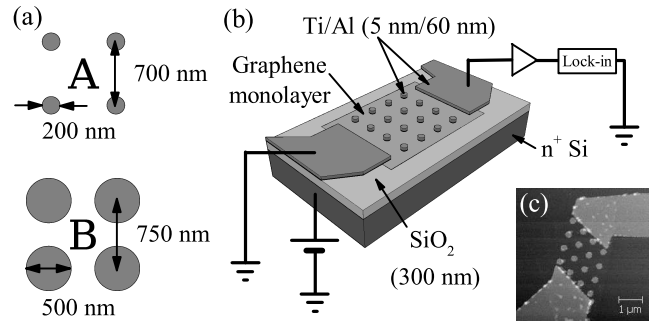


FIG. 1. (a) Schematics of array unit cells for device A (upper) and device B (lower). (b) Schematic of device A and two-terminal measurement circuit. (c) Atomic force microscope image of a similar device (disk diameter = 200 nm).

away from the graphene Dirac point. We also detect the presence of proximity vortices in the graphene through changes in the magnetoconductance whenever the magnetic field generates an integer number of flux quanta through the arrays.

Our graphene flakes are mechanically exfoliated from natural graphite onto degenerately doped Si substrates with a 300 nm oxide layer. We identify monolayer flakes by their optical contrast and quantum Hall measurements, then pattern superconducting electrodes and square arrays of disks using electron beam lithography followed by thermal evaporation of a Ti/Al bilayer (5 nm/60 nm) [Fig. 1]. We present measurements of two array geometries: device A has disks with diameter $2a = 200$ nm and center-center separation $b = 700$ nm, device B has disks with $2a = 500$ nm and $b = 750$ nm.

Two-, four- and quasi-four-terminal differential conductance was measured using standard low frequency AC lock-in techniques, in a pumped ³He cryostat at 340 mK

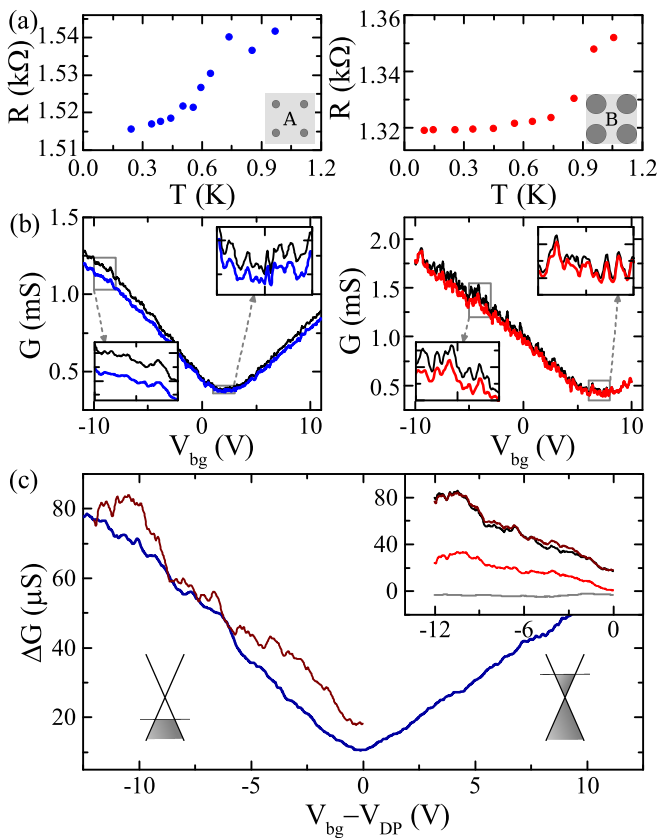


FIG. 2. (a) Temperature dependence of the zero-field differential resistance in devices A (left) and B (right). (b) Back-gate voltage (V_{bg}) dependence of the differential conductance at zero field (thin black) and above the critical field of each device (thick blue/red), $T = 350$ mK, for devices A and B, respectively. Grey boxes indicate data in insets. (c) Difference between the zero-field and critical-field conductance, ΔG , as a function of back-gate voltage relative to the Dirac point (thick dark blue: device A, thin dark red: device B). Inset: Temperature dependence of ΔG , device B. $T = 100$ mK (black), 350 mK (dark red), 750 mK (red) and 1.05 K (grey).

and a dilution refrigerator between 1.05 K and 100 mK. A voltage V_{bg} applied to the doped Si substrate controlled the carrier density. For devices A and B, the graphene exhibited a Dirac point at $V_{bg} \approx 2$ V and 6 V and a carrier mobility of ~ 3500 $\text{cm}^2(\text{Vs})^{-1}$ and ~ 5400 $\text{cm}^2(\text{Vs})^{-1}$ for $n = 5 \times 10^{11}$ cm^{-2} and $T = 350$ mK. The electron mean-free path $l_e = 2D/v_F$ is approximately 130 nm for device A and 90 nm for device B, where D is the diffusion constant (≈ 0.03 m^2s^{-1} and 0.05 m^2s^{-1}).

Figure 2(a) shows the zero-field resistance of both devices as a function of temperature. We observe a pronounced decrease in both cases below the critical temperature of the Ti/Al bilayer, which is around 1 K. A similar decrease in resistance was recently reported [9] and attributed to the absence of dissipation from regions under and around the disks due to the proximity effect [10]. The percentage decrease we see is not proportional to

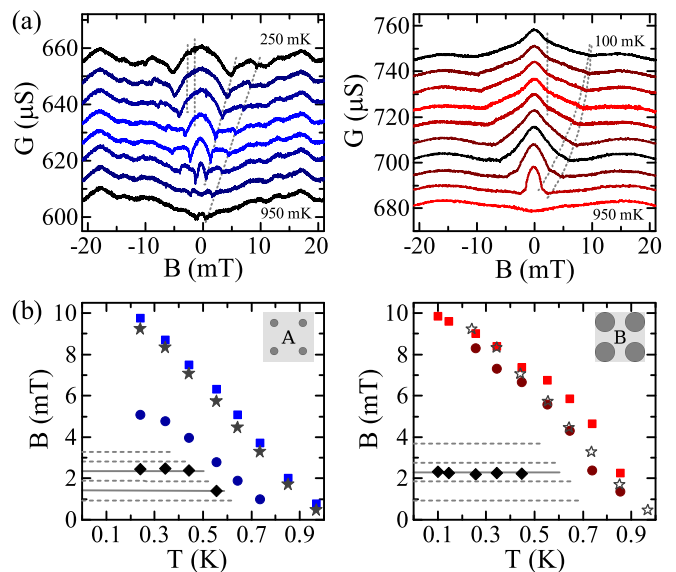


FIG. 3. (a) Magnetoconductance at temperatures between 250 mK and 950 mK (100 mK and 150 mK traces also shown for device B). Traces offset for clarity, grey dashed lines highlight features plotted below. (b) Plots of the critical field of the Ti/Al bilayer (stars), outermost (squares) and innermost (circles) temperature-dependent features, and temperature-independent features (diamonds). Grey horizontal lines are rational fractions of flux quanta per array unit cell; $\frac{2}{9}$ to $\frac{7}{9}$ in left panel, $\frac{1}{4}$ to $\frac{4}{4}$ and $\frac{5}{8}$ in right panel.

the percentage of the graphene covered by the disks, limited perhaps by interface conductance or potential barriers between covered and uncovered regions of graphene. However, the temperature at which the resistance drops is higher for device B. Since the edge-to-edge separation of the disks is smaller in this device, this would indicate a proximity effect in the arrays [11]. We do not observe a fully superconducting state, even at the lowest temperatures. Although in theory the transition to the full proximity effect can be tuned by the back-gate in graphene [7], in practice the low critical temperature of aluminium restricts the T/T_c range of our measurements.

Figure 2(b) plots the conductance of both devices above and below the critical field of the disks as a function of back-gate voltage. In Fig. 2(c), we find that the conductance enhancement due to the presence of superconductivity in the leads and islands depends linearly on the carrier density (in contrast to Ref. [9]). We attribute this to the greater diffusion of carriers around the contacts at higher carrier density, and a corresponding increase in the area of the effectively gapped region. As the temperature is increased [inset of Fig. 2(c)] the linear dependence on back-gate voltage persists, and by $T = 750$ mK the magnitude of ΔG has approximately halved. Above the critical temperature of the leads, ΔG is small and negative due to the suppression of weak localisation [12].

Having established that the modulation of the resistance is consistent with proximity effects around the islands, we now describe the magnetoconductance. Figure 3(a) shows the field-dependent differential conductance, captured at different temperatures, for devices A and B. In both devices, the application of a small magnetic field below T_c decreases the conductance of the arrays up to a critical field and for a wide range of carrier densities in both the electron and hole conduction regimes. Close inspection of these data reveals both temperature-dependent and -independent features, plotted in Fig. 3(b). Also plotted, for reference, is the critical field of branched contacts on device A. Note that sub-micron Al islands have been shown to have the same properties as continuous films [13], suggesting the disks have the same critical field and temperature as the leads.

The first set of temperature-dependent features closely follows the critical field of the Ti/Al bilayer in both devices. The second set appears at lower fields and has a similar temperature dependence, but differs in magnitude between devices, occurring at smaller fields and temperatures in device A. This correlation indicates that the two sets of features are related to the extent of the proximity effect in the graphene. Below the critical field of the disks it is likely that Andreev reflection at the interfaces affects transport, explaining the first set of features. The second set corresponds to phase coherence between neighbouring pairs of disks. The dephasing length estimated from the weak localisation peak is approximately 200 nm at $T = 950$ mK in both devices, and therefore spans the region between disks first in device B, then in device A as the temperature decreases. Phase coherence between neighbouring pairs of disks implies a full proximity effect and hence dissipationless path between them, leading to the observed increase in conductance below the second set of temperature-dependent features.

Below the second temperature-dependent feature, we observe temperature-independent features at fields which appear to be related to the area of the array unit cell. These have been highlighted in Fig. 3(b). Such features at fixed fields are expected in two-dimensional Josephson junction arrays [14, 15], due to low-energy configurations of vortices within the array, such as integer numbers of flux quanta per unit cell, or a superlattice of empty and occupied cells. We observe temperature-independent features at $\frac{1}{3}$ and $\frac{5}{9}$ for device A and $\frac{5}{8}$ for device B, whereas in a large, square array the lowest energy configurations correspond to fields of $\frac{n}{4}$ flux quanta per unit cell [16].

To examine these features in more detail, and eliminate universal conductance fluctuations and any normal state conductance dependence, we average over a 20V range of back-gate voltage, and plot the results in Fig. 4(a). We find features at fields of $\frac{n}{9}$ flux quanta per unit cell for device A, and $\frac{n}{4}$ for device B. Figure 4(b) and (c) shows the absolute numerical derivative of the back-gate-averaged resistance of device A as a function of flux

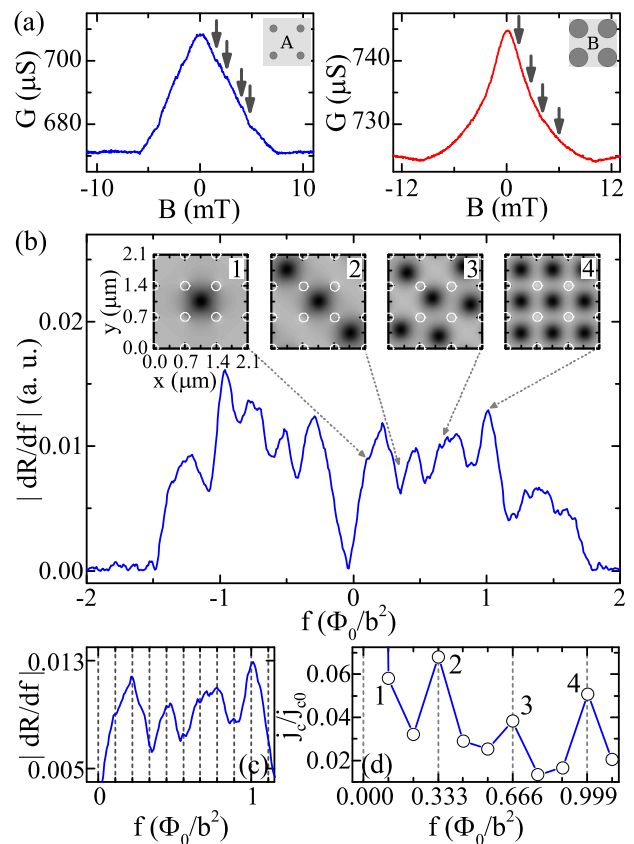


FIG. 4. (a) Magnetoconductance at $T = 350$ mK, averaged over back-gate voltage. Arrows indicate features at rational fractions of flux quanta per array unit cell, f . (b) Derivative of the back-gate-averaged resistance of device A as a function of f . Panels 1–4: Local magnetic field distribution in device A (black = high field, grey = low field) calculated using the Ginzburg-Landau formalism, at applied fields indicated by arrows. White circles show disk locations. (c) Data from (b), with grey vertical lines indicating $\frac{n}{9}$ flux quanta per unit cell. (d) Calculated critical current as a function of flux quanta per unit cell, normalised to the zero-field value. Numbered points correspond to panels 1–4. Ginzburg-Landau results are obtained at $T = 0.9T_c$ for anisotropy coefficient $g(r) = 0.25$, coherence length $\xi(0) = 20$ nm, and penetration depth $\lambda(0) = 200$ nm.

quanta per unit cell. Grid lines at $\frac{n}{9}$ in Fig. 4(c) align with the features, confirming our earlier observation of temperature-independent features in the raw magnetoconductance.

To understand why the features occur at fields of $\frac{n}{9}$ flux quanta per unit cell in device A, rather than $\frac{n}{4}$, we perform simulations based on the Ginzburg-Landau equations. The model system is a square, 3×3 unit cell array of superconducting disks ($2a = 200$ nm, $b = 700$ nm) embedded in a normal metal matrix. The proximity effect is described by a spatially-dependent, anisotropic expansion coefficient of the Gibbs free energy functional, $\alpha = \alpha_0 g(r)$, which equals 1 inside the superconducting

disks and less than 1 in the metallic regions [17]. The square simulation region has periodic boundary conditions in all directions in the two-dimensional plane, and is exposed to a homogeneous magnetic field B . Figure 4(b), panels 1–4 show ground-state vortex configurations in the form of local magnetic field density, obtained in field-cooled simulations [18] since the initial vortex structure directly influences the response of the system to an applied current [19]. The critical depinning current j_c is then calculated by slowly driving a current through the system [20]. The critical current exhibits peaks at fields of $\frac{2}{3}$ flux quanta per unit cell [Fig. 4(d)], suggesting that the field values of the features in device A are due to the odd number of unit cells.

Along with the phase frustration effects detailed above, the presence of reproducible, aperiodic conductance fluctuations in our mesoscale flakes is a precursor of the superconducting glass state predicted [8] and recently observed [9] in graphene Josephson junction arrays. In Fig. 5 we explore the effect of the superconducting disks on universal conductance fluctuations (UCFs). Figure 5(a)

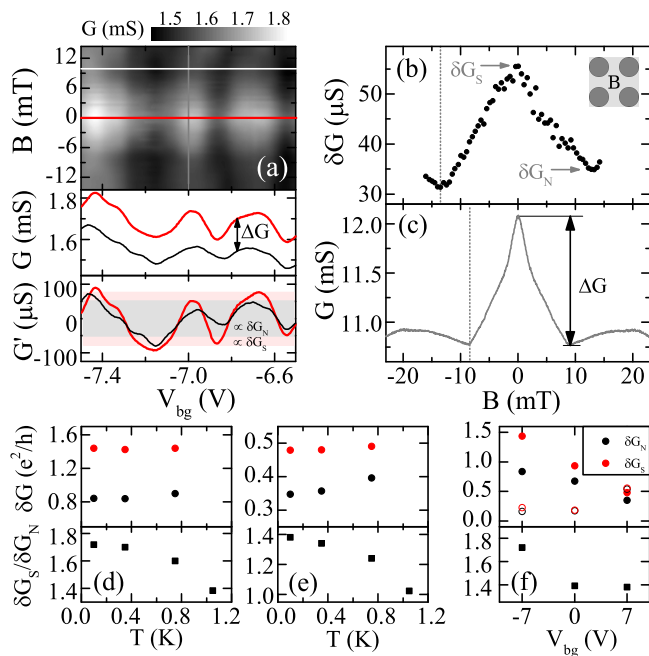


FIG. 5. $T = 100$ mK, $V_{bg} - V_{DP} = -14$ V unless stated otherwise. (a) Differential conductance of device B as a function of back-gate voltage and magnetic field (thick red lines: $B = 0$, thin black lines: $B = 10$ mT, G' is the detrended conductance). (b) Standard deviation of universal conductance fluctuations as a function of magnetic field; δG_N and δG_S are the values at $B = 10$ and 0 mT. (c) Differential conductance as a function of magnetic field (d), (e) Upper panel: Temperature dependence of δG_N (black) and δG_S (red) in terms of conductance quanta at $V_{bg} - V_{DP} = -14$ V and 0 V, respectively. Lower panel: Ratio of δG_S and δG_N . (f) As for (d) and (e), but showing carrier density dependence at 100 mK (solid markers) and 1.05 K (hollow markers).

shows UCFs in device B as a function of back-gate voltage and applied field, at $T = 100$ mK and $V_{bg} - V_{DP} = -14$ V. The overall conductance of the array is enhanced below the critical field of the leads (middle panel), however, the UCFs themselves are also enhanced, as seen in the detrended conductance (lower panel). Figure 5(b) shows the standard deviation of the UCFs, $\delta G = \sqrt{\langle G^2 \rangle - \langle G \rangle^2}$, as a function of magnetic field. Below the critical field of the leads, δG increases linearly in magnitude towards zero-field. We observe this linear trend at different carrier densities and temperatures. Comparison of δG with the differential conductance of the device [Fig. 5(c)] reveals that δG is enhanced over a larger field range than the mean conductance.

Figure 5(d)-(f) quantifies the enhancement of δG between $B = 0$ (δG_S) and $B = 10$ mT (δG_N), and compares data taken at different back-gate voltages and temperatures. Upper panels show the values of δG_S and δG_N , and lower panels their ratio. The form of the temperature dependence is the same at both high and low carrier density [Fig. 5(d) and (e)]. Figure 5(f) shows the back-gate voltage dependence at 100 mK, and above the critical temperature of the leads at 1.05 K. The enhancement of ~ 1.4 – 1.7 is close to that observed in InAs nanowires [21] and graphene [22] contacted by Ti/Al bilayers. At 100 mK, δG is more enhanced away from the Dirac point. At 1.05 K, we observe the opposite trend in δG_N , with no enhancement at zero-field.

The enhancement of UCFs in mesoscopic devices with superconducting contacts is associated with Andreev reflection at the normal/superconductor interface [23]. The temperature-dependence of the UCF enhancement, and its onset at larger applied fields compared to the mean conductance, can be linked to the superconducting gap in the Ti/Al bilayer. A larger gap implies more Andreev reflection at the interfaces, and therefore greater enhancement of the UCFs. Our observation of a smaller enhancement close to the Dirac point is more intriguing, since suppression of superconductivity near the graphene Dirac point has been seen before in large-area devices [9, 24]. So far, the suppression has only been seen in the global conductance, but it also appears here in conductance fluctuation data. Loss of phase coherence caused by the formation of electron-hole puddles at low carrier densities [25] may be responsible for the suppression in both global conductance and fluctuations [24]. A simple normal-state resistance dependence is unlikely, since the ratio of δG_S and δG_N is the same at $V_{bg} - V_{DP} = -7$ V and the Dirac point, nor is our square resistance high enough for a metal-superconductor transition [7, 9]. Another possibility is the loss of Andreev pairs due to specular Andreev reflection at the graphene/disk interfaces [26], though a measurable contribution is unlikely given the diffusive transport in our substrate-supported graphene.

In summary, we have explored the interplay between

normal-state and superconducting phase effects in ordered arrays of mesoscopic superconductors on graphene. Even without a full proximity effect spanning the device, magnetoconductance features at rational fractions of flux quanta per array unit cell indicate the presence of proximity vortices. We also observe suppression of the proximity effect at the Dirac point through the mean conductance and conductance fluctuations, due to the phase-breaking effect of disorder-induced charge puddles in our large-area devices, or perhaps a contribution from specular Andreev reflection at the graphene/disk interfaces.

These measurements of graphene-based Josephson junction arrays demonstrate the feasibility of detecting and manipulating superconducting vortices in Dirac conductors through charge transport. Extension of this approach to topological insulators could be a route to detection of non-Abelian statistics and implementation of topological quantum computing.

This work was financially supported by the Engineering and Physical Sciences Research Council, and an NPL/EPSC Joint Postdoctoral Partnership (RG61493).

-
- [1] R. Jackiw and P. Rossi. Zero modes of the vortex-fermion system. *Nucl. Phys. B*, 190(4):681 – 691, 1981. ISSN 0550-3213.
- [2] Liang Fu and C. L. Kane. Superconducting proximity effect and majorana fermions at the surface of a topological insulator. *Phys. Rev. Lett.*, 100:096407, 2008.
- [3] Liang Fu and C. L. Kane. Josephson current and noise at a superconductor/quantum-spin-hall-insulator/superconductor junction. *Phys. Rev. B*, 79:161408, 2009.
- [4] Pouyan Ghaemi and Frank Wilczek. Near-zero modes in superconducting graphene. *Phys. Scripta*, 2012(T146):014019, 2012.
- [5] H. B. Heersche, P. Jarillo-Herrero, J. B. Oostinga, L. M. K. Vandersypen, and A. F. Morpurgo. Bipolar supercurrent in graphene. *Nature*, 446:56–59, 2007.
- [6] B. M. Kessler, Ç. Ö. Girit, A. Zettl, and V. Bouchiat. Tunable superconducting phase transition in metal-decorated graphene sheets. *Phys. Rev. Lett.*, 104:047001, 2010.
- [7] A. Allain, Z. Han, and V. Bouchiat. Electrical control of the superconducting-to-insulating transition in graphene/metal hybrids. *Nat. Mater.*, 11:190–194, 2012.
- [8] M. V. Feigel'man, M. A. Skvortsov, and K. S. Tikhonov. Proximity-induced superconductivity in graphene. *JETP Lett.*, 88:747–751, 2008.
- [9] Zheng Han, Adrien Allain, Hadi Arjmandi-Tash, Konstantin Tikhonov, Mikhail Feigel'man, Benjamin Sacépé, and Vincent Bouchiat. Collapse of superconductivity in a hybrid tin-graphene Josephson junction array. *Nat. Phys.* advance online publication, 30 March 2014.
- [10] D. J. Resnick, J. C. Garland, J. T. Boyd, S. Shoemaker, and R. S. Newrock. Kosterlitz-thouless transition in proximity-coupled superconducting arrays. *Phys. Rev. Lett.*, 47:1542–1545, 1981.
- [11] S. Eley, S. Gopalakrishnan, P. M. Goldbart, and N. Mason. Approaching zero-temperature metallic states in mesoscopic superconductor-normal-superconductor arrays. *Nat. Phys.*, 8:59–62, 2012.
- [12] E. McCann, K. Kechedzhi, Vladimir I. Fal'ko, H. Suzuura, T. Ando, and B. L. Altshuler. Weak-localization magnetoresistance and valley symmetry in graphene. *Phys. Rev. Lett.*, 97(14):146805, 2006.
- [13] A. K. Geim, I. V. Grigorieva, S. V. Dubonos, J. G. S. Lok, J. C. Maan, A. E. Filippov, and F. M. Peeters. Phase transitions in individual sub-micrometre superconductors. *Nature*, 390:259–262, 1997.
- [14] S. Teitel and C. Jayaprakash. Josephson-junction arrays in transverse magnetic fields. *Phys. Rev. Lett.*, 51:1999–2002, 1983.
- [15] A. T. Fiory, A. F. Hebard, and S. Somekh. Critical currents associated with the interaction of commensurate fluxline sublattices in a perforated film. *Appl. Phys. Lett.*, 32(1):73–75, 1978.
- [16] H. S. J. van der Zant, M. N. Webster, J. Romijn, and J. E. Mooij. Vortices in two-dimensional superconducting weakly coupled wire networks. *Phys. Rev. B*, 50:340–350, 1994.
- [17] G.R. Berdiyrov, A.R. Romaguera, M.V. Milošević, M.M. Doria, L. Covaci, and F.M. Peeters. Dynamic and static phases of vortices under an applied drive in a superconducting stripe with an array of weak links. *Eur. Phys. J. B*, 85:1–8, 2012. ISSN 1434-6028.
- [18] G. R. Berdiyrov, M. V. Milošević, and F. M. Peeters. Novel commensurability effects in superconducting films with antidot arrays. *Phys. Rev. Lett.*, 96:207001, 2006.
- [19] M. L. Latimer, G. R. Berdiyrov, Z. L. Xiao, W. K. Kwok, and F. M. Peeters. Vortex interaction enhanced saturation number and caging effect in a superconducting film with a honeycomb array of nanoscale holes. *Phys. Rev. B*, 85:012505, 2012.
- [20] G. R. Berdiyrov, M. V. Milošević, and F. M. Peeters. Superconducting films with antidot arrays—novel behavior of the critical current. *Europhys. Lett.*, 74(3):493, 2006.
- [21] Yong-Joo Doh, Silvano De Franceschi, Erik P. A. M. Bakkers, and Leo P. Kouwenhoven. Andreev reflection versus coulomb blockade in hybrid semiconductor nanowire devices. *Nano Lett.*, 8(12):4098–4102, 2008.
- [22] J. Trbovic, N. Minder, F. Freitag, and C. Schönenberger. Superconductivity-enhanced conductance fluctuations in few-layer graphene. *Nanotechnology*, 21(26):A264005, 2010.
- [23] C. W. J. Beenakker. Random-matrix theory of quantum transport. *Rev. Mod. Phys.*, 69(3):731, 1997.
- [24] K. Komatsu, C. Li, S. Autier-Laurent, H. Bouchiat, and S. Guéron. Superconducting proximity effect in long superconductor/graphene/superconductor junctions: From specular andreev reflection at zero field to the quantum hall regime. *Phys. Rev. B*, 86:115412, 2012.
- [25] J. Martin, N. Akerman, G. Ulbricht, T. Lohmann, J. H. Smet, K. von Klitzing, and A. Yacoby. Observation of electron-hole puddles in graphene using a scanning single-electron transistor. *Nat. Phys.*, 4:144–148, 2008.
- [26] C. W. J. Beenakker. Specular andreev reflection in graphene. *Phys. Rev. Lett.*, 97:067007, 2006.